Supporting Information

Multi-Sensor Remote Sensing Evidence of Connection between Deep Aquifer Recharge in California's Central Valley and Sierra Nevada Snowmelt

Susanna Werth[1,2], Manoochehr Shirzaei[1,2,3], Grade Carlson[1,4], and Roland Bürgmann[5]

[1]Virginia Tech, Department of Geosciences, Blacksburg, VA, USA.
[2]Virginia Tech, National Security Institute, Blacksburg, VA, USA.
[3]United Nations University, Institute for Water, Environment and Health, Hamilton, ON L8P 0A1, Canada
[4]Indiana University, Department of Geography, Bloomington, IN, USA
[5]University of California, Berkeley, Department of Earth and Planetary Science, Berkeley, CA, USA.

Correspondence to: Susanna Werth (swerth@vt.edu)

Contents of this file

Introduction

This supplemental material contains additional information in the form of text and figures about deformation in unconfined aquifers due to groundwater level change and Figures with further details about meteorological, GNSS, and GWL data, as well as uncertainty analyses, which are discussed in the main text.

Text S1. Poroelastic Deformation of Unconfined Aquifers

Poroelastic deformation in unconfined aquifers due to changes in groundwater levels exists, but it is much smaller and below a measurable amplitude compared to confined aquifers. Water in unconfined aquifers is released from drainage but not from aquifer compaction or water expansion, as it is in confined aquifers.

To test if the shallower units may contribute significantly to the elastic subsidence, we calculate the subsidence signal related to water level decrease in shallow unconfined aquifers, using the 1-D consolidation model of Terzaghi (detailed in Ojha et al., 2018). The aquifer compaction (db) is given by:

$$db = \frac{b \times \alpha_B \times \rho_w \times g \times dh}{E} \quad \text{(S1)}$$

where b is the thickness of the shallow aquifer that is recharged due to precipitation, we generously assume it to be 10 m (which is an upper bound and usually is less than a few meters), ρ_w is water density, g is the gravitation acceleration, dh is change in water table due to discharge, which we assume to be also 10 m, namely the entire aquifer is emptied, E is the static bulk modules, which we assume to be 150 MPa after Ojha (2018). α_B is the Biot-Willis coefficient, defined as the ratio of volume of fluid that is added to the aquifer divided by the change in the bulk volume under constant pore pressure, which ranges between 0 (unconfined) and 1 (confined). We set the Biot-Willis coefficient to be 0.2 for the shallow sandy-clay layers in the San Joaquin Valley. The value of elastic subsidence, db, is 1 mm. This value is below the uncertainty of InSAR and GNSS measurements used in here, and thus, we conclude the observed elastic subsidence cannot be due to water level decreases in shallow unconfined aquifers.

Text S2. Physical discrimination of pressure and storage propagation in aquifers

While related, pressure (or pressure propagation) and storage (or mass) changes are physical phenomena governed by distinct mathematical equations and occur on different time scales. The temporal evolution of pressure ($\frac{dP}{dt}$) follows:

$$\frac{dP}{dt} = \kappa \cdot \nabla^2 P \,, \quad \text{(S2)}$$

where the hydraulic diffusivity $\kappa = K/S_s$, controling the speed of pressure propagation, is the ratio of vertical hydraulic conductivity K to specific storage S_s.

On the other hand, the law governing groundwater flow (i.e., mass transport) is provided by Darcy's equation:

$$q = -K \cdot \nabla P, \quad \text{(S3)}$$

where q is flux per unit area and assuming groundwater volume flow $Q = q \cdot A$ and with $K = \kappa \cdot S_S$ Equation (3) can be rewritten as:

$$Q = \frac{dV}{dt} = -\kappa \, S_S \, A \cdot \nabla P \,. \quad \text{(S4)}$$

Equation 4 illustrates that the groundwater flow depends on the cross-sectional area of the flow path and the specific storage coefficient, both of which are small for the mountain block. For fractured bedrock S_S has magnitudes as small as 10^{-5} to 10^{-6}.

In contrast, pressure propagation is independent of these two factors. Hence, the recovery of water storage in the valley due to water transport from the mountain through fractures must take much longer than the propagation of the pressure front (Viswanathan et al., 2022).

At the timescale of months, this can change the pressure head without significantly affecting the valley storage. However, in this study, we are primarily interested in the annual propagation of a pressure front driven by snow melt and winter rain. Hence, we only make a first-order feasibility assessment on the time required for a pressure front to propagate vertically from the mountains to deep layers (i.e., depths below the Corcoran clay) of the valley aquifer system (see Supplementary Text S3 for details).

Text S3. Technical details on the first-order assessment of pressure propagation from mountains to deep aquifers

Here, to obtain the first-order approximation of the diffusion time, namely the time it takes for snow melt-related pore-fluid pressure increase in the Sierra to reach deep aquifer layers of the CV via MBR, we apply the 1D form of Equation 1 of the main manuscript following (Saar & Manga, 2003). Hence, the vertical propagation of hydrostatic pore-fluid pressure P at depth z over time t is governed by the diffusion equation:

$$\kappa \frac{\partial^2 P}{\partial z^2} = \frac{dP}{dt} . \quad \text{(S5)}$$

and the hydraulic diffusivity κ controls how fast pressure will propagate to depth. The diffusivity of unfractured granite bedrock has values of around $\kappa = 10^{-4}\ m^2/s$ (Wang, 2000). However, for fractured volcanic rock, values as high as 0.3 m^2/s (Saar & Manga, 2003), and 1 m^2/s (Gao et al., 2000), consistent with the range provided by Talwani and Acree (1985), or even up to 7.9 m^2/s (Montgomery-Brown et al., 2019) are suggested. The true diffusivity values are highly uncertain, as MBR likely occurs through conduits with secondary porosity, and their contribution may be underestimated at a large scale and, therefore, not be reflected accurately in local studies. Here, we use ranges of diffusivity provided in recent works pointing to a higher importance of mountain block recharge than previously assumed. We consider diffusivity values of 0.1, 0.3, and 0.5 m^2/s for Sierra's crystalline fractured rocks. We also consider depths of 600-2000 m, corresponding to the vertical distance from the high mountains to the deep aquifer layers below the Corcoran clay. This estimate is derived from the elevation difference between the western Sierra Nevada recharge areas and the valley floor, combined with the approximate depth of deeper aquifer layers below confining units.

We solve the parabolic differential Equation 5 using the function *pdepe*() from the Matlab software by setting the initial pressure conditions to zero and the boundary conditions of the pore-fluid pressure at the top of the aquifer to a periodic variation with periodicity ψ of 1 year, annual amplitude P_{max} and annual phase φ_0:

$$P'_{z,t=0} = P_{max} \cdot \cos\left(\frac{2\pi}{\psi} t + \varphi_0\right) \quad \text{(S6)}$$

where at depth z, pore-fluid pressure is $P_{z,t} = P_{z,t-1} + P'_{z,t}$. We are only interested in changes $P'_{z,t}$ of pore-fluid pressure. We do not introduce a boundary condition at the bottom of the aquifer.

Assuming saturated conditions and solving Equations 5 and 6 for t allows us to estimate the time it takes to increase pore-fluid pressure annually due to groundwater recharge reaching vertically from top groundwater layers to depth. The duration of pressure propagation to deep aquifer layers is independent of the amplitude of pressure change at the surface and a normalized solution for $P'_{z,t=0}/P_{max}$ is sufficient. The time delay estimate is most sensitive to the magnitude of the hydraulic diffusivity κ (Eq. 4) as well as the phase φ_0, of the annual pressure variation due to recharge (Eq. 5). We further assume that the horizontal diffusivity of the aquifer is large enough, and despite the width of the valley and hydrological complexities, it is likely that the lateral diffusion rate is relatively small, compared to the vertical diffusion rate (Fetter & Kreamer, 2022).

The annual phase of pressure variations in upper groundwater layers in the high Sierra Nevada φ_0 may be derived from the annual variation in available water for recharge in this region, which we quantify as follows. Here, we refer to the upper parts of the mountain block connected to the surface water supply, which experience increased water pressure during the rainy and melting seasons, with little delay. Hence, these top groundwater layers in the Sierra Nevada receive inflow from snowmelt and liquid precipitation (i.e., rainfall). Urióstegui et al. (2017) and Bales et al. (2011) found that only 10-20% of the snowmelt water in the Sierra Nevada runs off through streams, with the remainder being lost to drainage into deep layers and evapotranspiration. We assume that all of the meltwater initially increases pressure in the upper groundwater layers of the Sierra Nevada before evaporating or running off. Also, we neglect the delay between the time that water for infiltration becomes available and its percolation into the upper groundwater layers of the Sierra Nevada. We consider these assumptions reasonable for large areas of exposed fractured bedrock, given that we are only interested in quantifying the phase, not the absolute magnitude of maximum pressure variations. For that, we retrieve the time series of SNODAS dataset variables 'snowmelt runoff at the base of the snowpack' M and 'liquid precipitation.' P_{liqu} (see Section 2.1, Fig. S1) averaged for the drainage area of the Sierra Nevada toward the CV (rose-shaded area in Fig. 1a). We correct liquid precipitation for canopy interception by a relative value of 20%, adapting this estimate from previous studies for mixed forests in the Sierra Nevada (Bales et al., 2011). This intercept changes the relative amplitudes between M and P_{liqu}, and therefore, it can impact the annual phase. Finally, we get a time series of total water available for recharge in the Sierra Nevada drainage area from $(P_{liqu} - 0.2 \cdot P_{liqu} + M)$ and quantify monthly mean values of this time series during 2002-2020 (Fig. S2c). We also determine the mean timing of the annual peak for each year and at each location in the drainage area, which we apply as the timing of the annual maximum of the pressure variation to constrain φ_0 for the boundary condition in Equation 6.

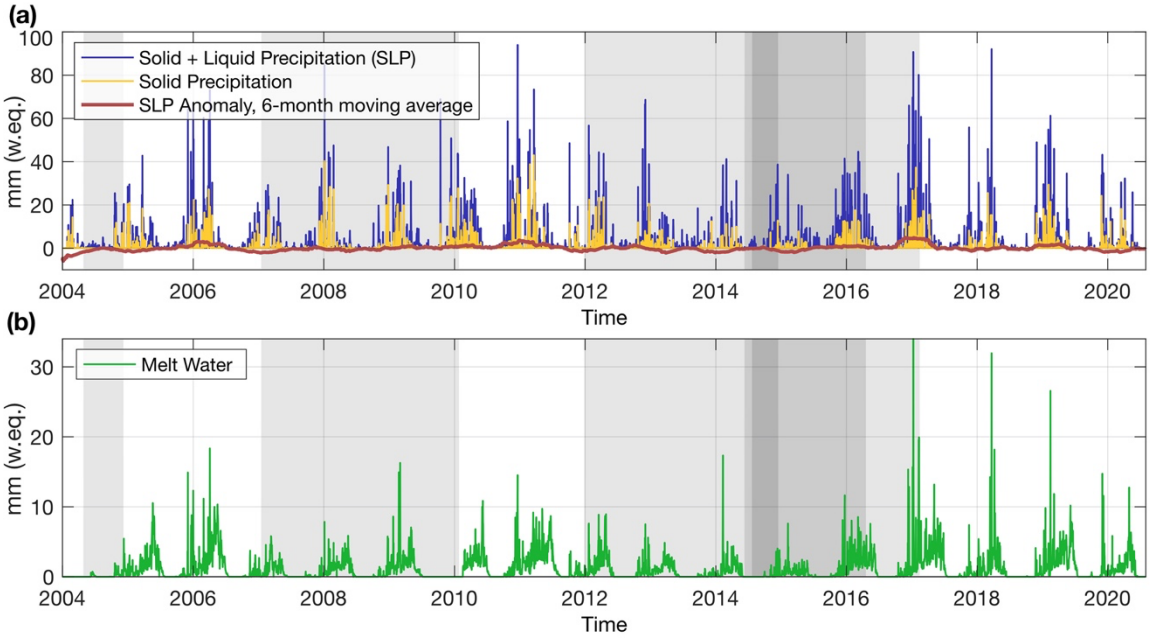

Figure S1. Precipitation and meltwater in the Sierra Nevada recharge area. (a) Daily time series of precipitation in the Sierra Nevada drainage area (rose shaded area in Fig. 1a) as retrieved from the SNODAS dataset. Shown is the sum of liquid and solid precipitation (blue), solid precipitation (yellow), and a 6-months moving average of monthly precipitation anomalies, which were estimated as difference between daily (liquid and solid) precipitation to average precipitation for a respective calendar day during the observation period 01/2004-07/2020. (b) Daily time series of SNODAS meltwater (green) for the same area. Gray shaded background areas (light, medium, dark gray) indicate that the USDM identifies >30% (>30%, >60%) of California's area to be in moderate (exceptional, exceptional) dry condition (compare Fig. S3).

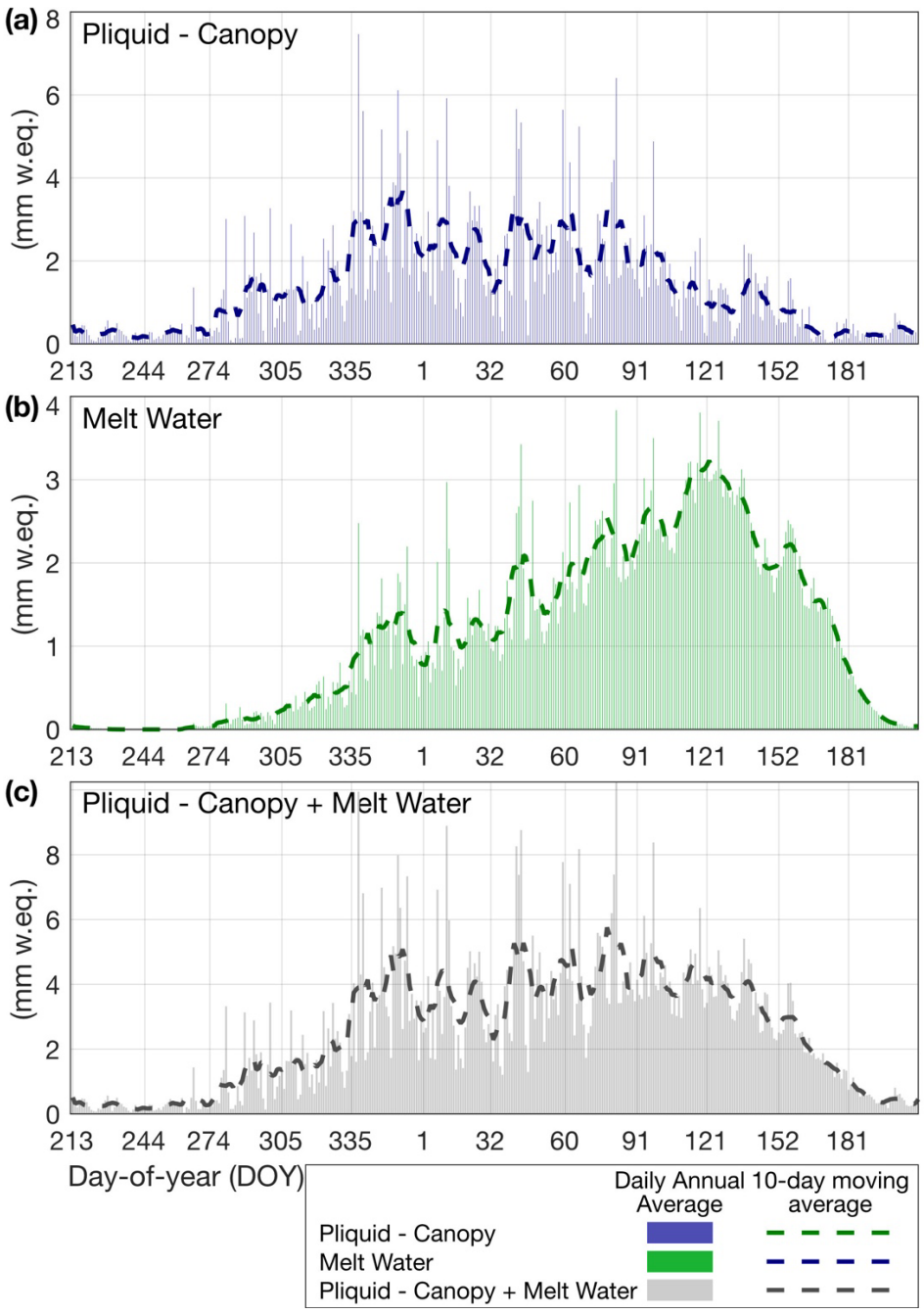

Figure S2. Water availability in the Sierra Nevada. Components of daily annual average water availability in the Sierra Nevada drainage area (rose shaded area in Fig. 1A), which were estimated as difference between daily SNODAS values and average values for a respective calendar day during the observation period 01/2004-07/2020. Values are shown as daily bars for (A) liquid precipitation corrected for canopy interception (20% of liquid precipitation), (B) meltwater, and (C) sum of liquid precipitation corrected for canopy interception plus meltwater. Dashed graphs show 10-day moving average of the respective bar graphs.

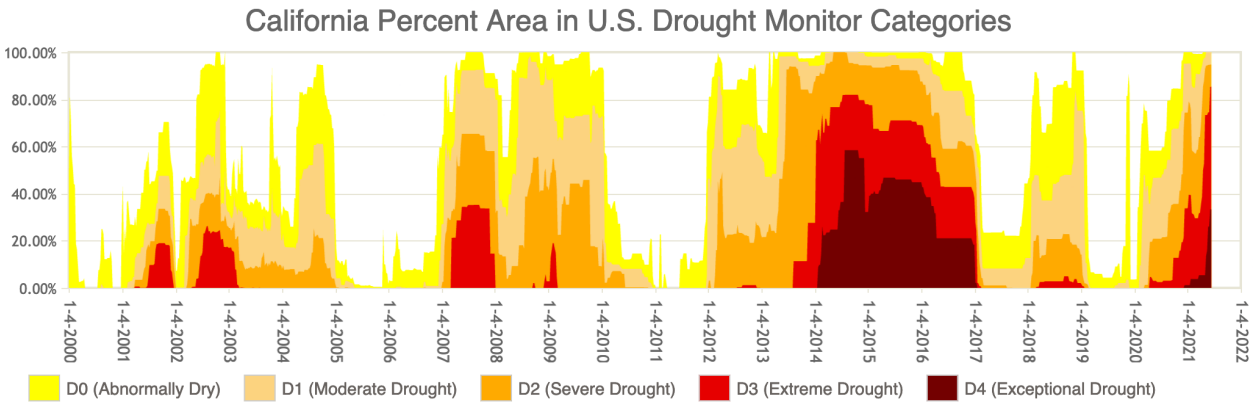

Figure S3. United States Drought Monitor for California. Temporal progression of drought severity in California, during 2000-2022, indicated a percentage of the state's area that experiences a certain drought severity. Different drought severity is indicated by different colors. The time series data were provided by the United States Drought Monitor (USDM) and retrieved from https://droughtmonitor.unl.edu. The U.S. Drought Monitor is jointly produced by the National Drought Mitigation Center at the University of Nebraska-Lincoln, the United States Department of Agriculture, and the National Oceanic and Atmospheric Administration. Map courtesy of NDMC.

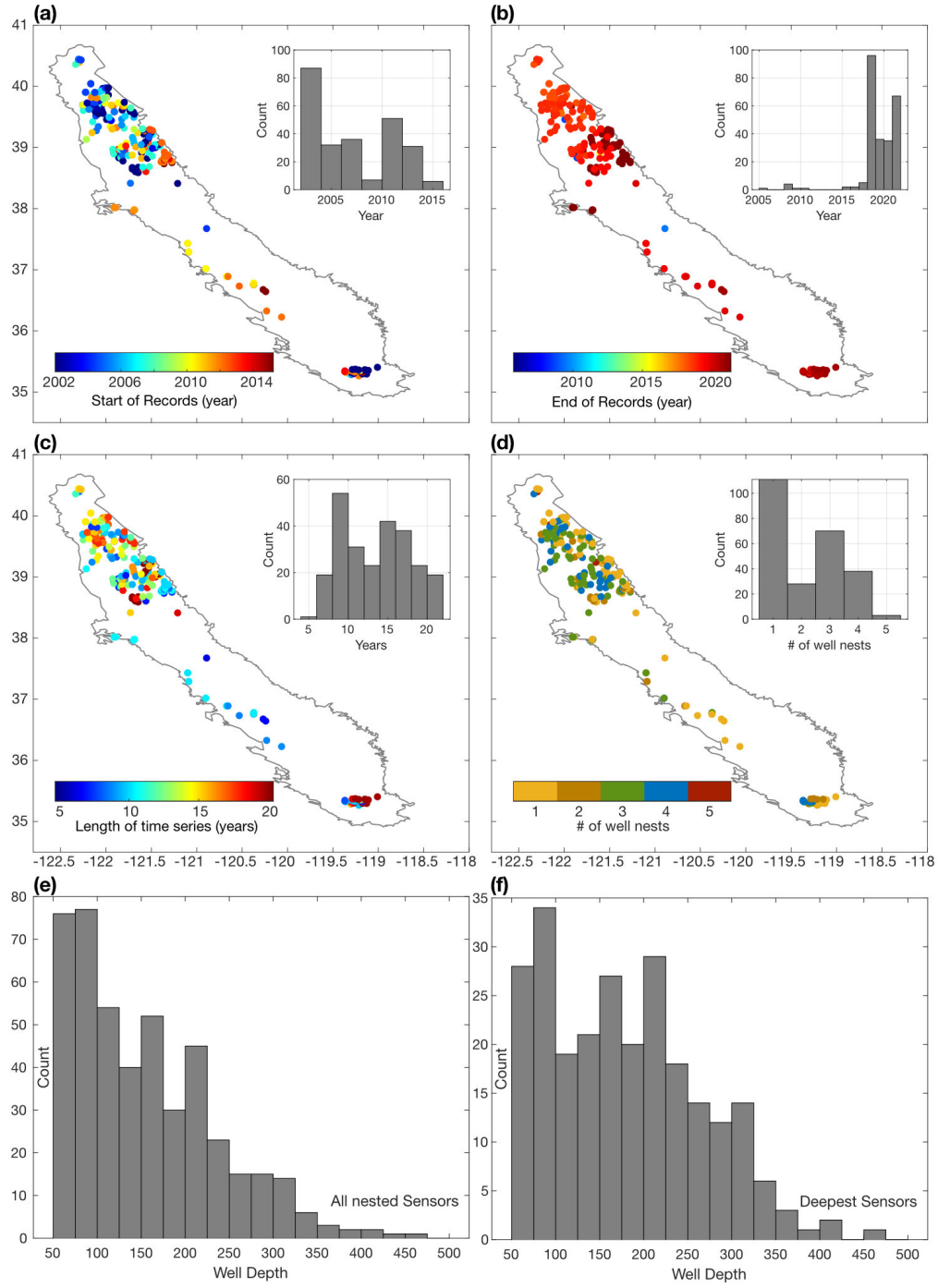

Figure S4. Groundwater well data. Availability of DWR and USGS groundwater level records at well sites with deepest sensor at depth of below 50 m throughout the Central Valley and corresponding histogram: (a) start year of records, (b) end year of records, (c) length of records in years, and (d) number of nested sensors at each observation well. (e) Histogram for number of sensors per depth, including all nested sensors (see d). (f) Histogram for number of sensors per depth only, including deepest sensor at any given site.

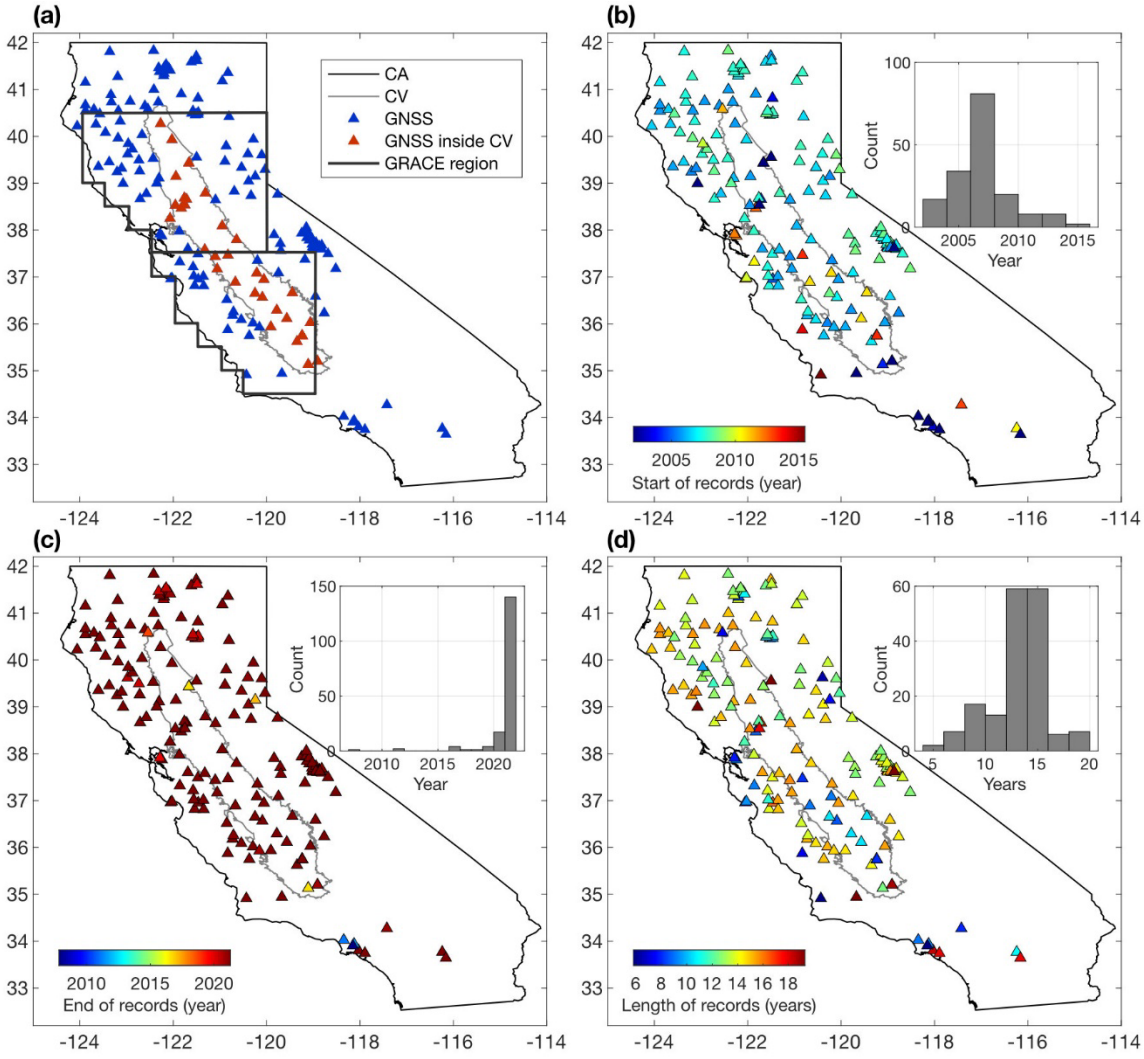

Figure S5. Overview of GNSS data availability. (a) Location of GNSS sites (same as Fig. 1b), (b) start year of GNSS time series, (c) end year of GNSS time series, and (d) length of GNSS time series in years.

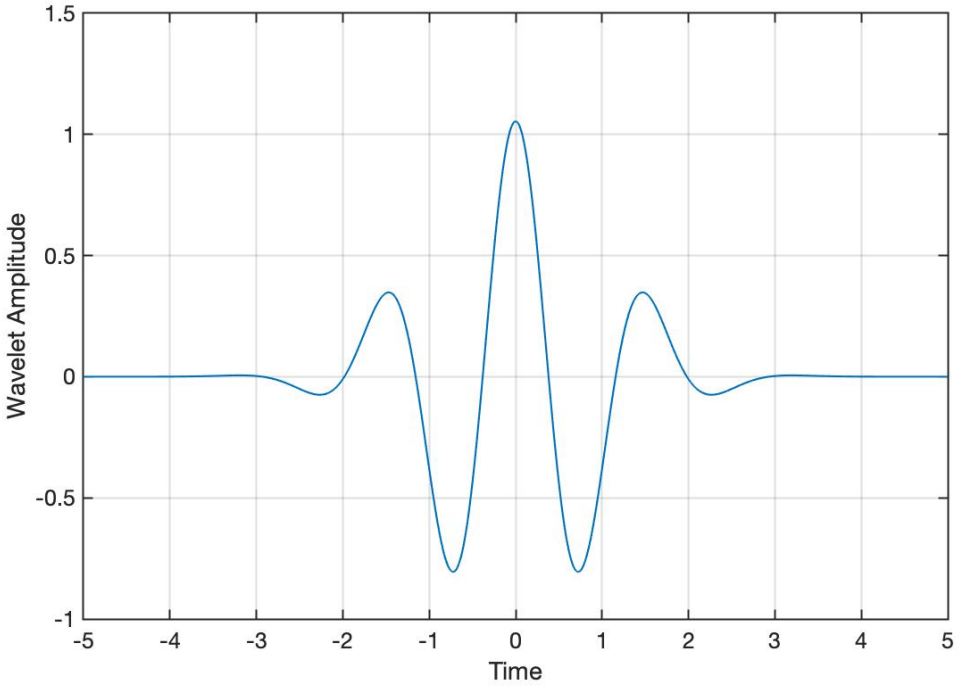

Figure S6. Wavelet Base Function. For the wavelet-based time-frequency analysis in this study, we apply a Derivative of Gaussian (DOG) as a wavelet base function. Shown here is a DOG of 8th order.

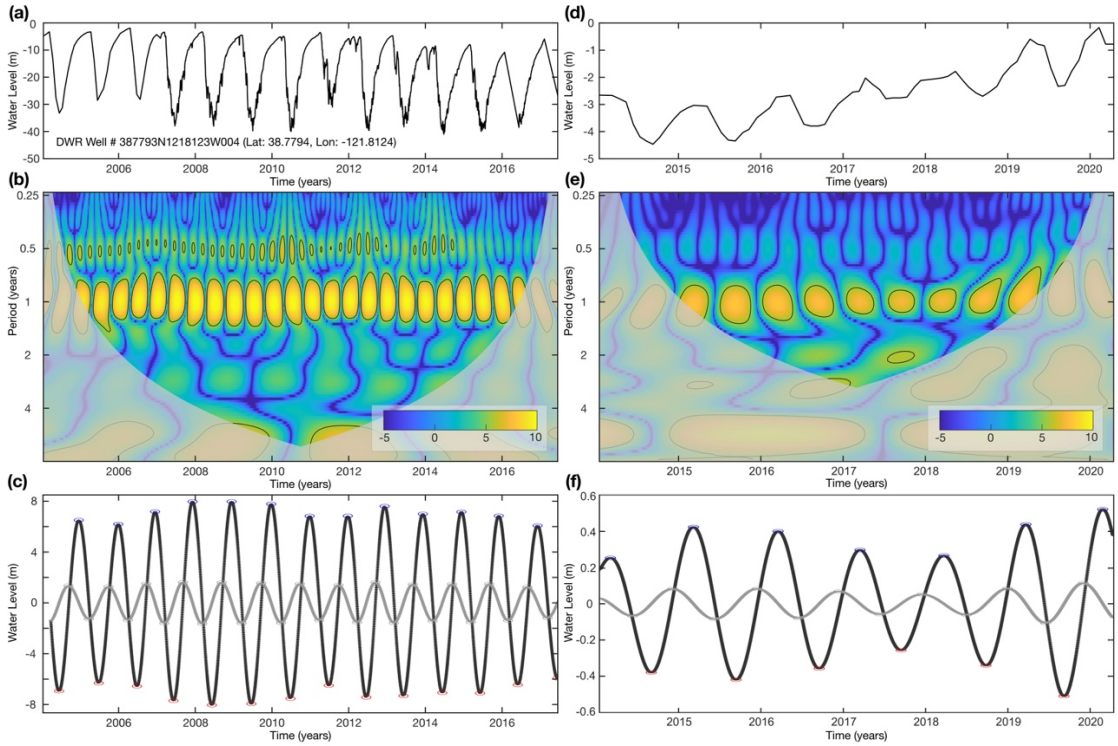

Figure S7. Example for isolating the annual signal component from a time series with wavelet analysis using DOG wavelets (Fig. S6) and for time series with different temporal sampling rates. (a) Example groundwater level time series as measured at the DWR well #387793N1218123W004 with daily temporal resolution and two gaps in 2016 and 2017 which were interpolated to daily sampling rate, (b) corresponding wavelet power spectrum with cone-of-influence (black thick line) and contour line for signal power above signal noise level (black thin lines), and (c) the determined seasonal signal component (black line) reconstructed from signal power exhibited at the period range of 0.75-1.25 years. (d-e) Same as a-c but for a groundwater level time series with monthly temporal resolution, here, as measured at the DWR well #387626N1213651W002. Blue and red ellipses identify annual maxima and minima. The gray line is the temporal derivative of the reconstructed annual signal, with maxima and minima indicating maximum increase or decrease in the annual signal. Data gaps longer than three months in the original time series are masked out in the reconstruction. Here, gaps in 2016 and 2017 are shorter and do not affect the seasonal signal's isolation.

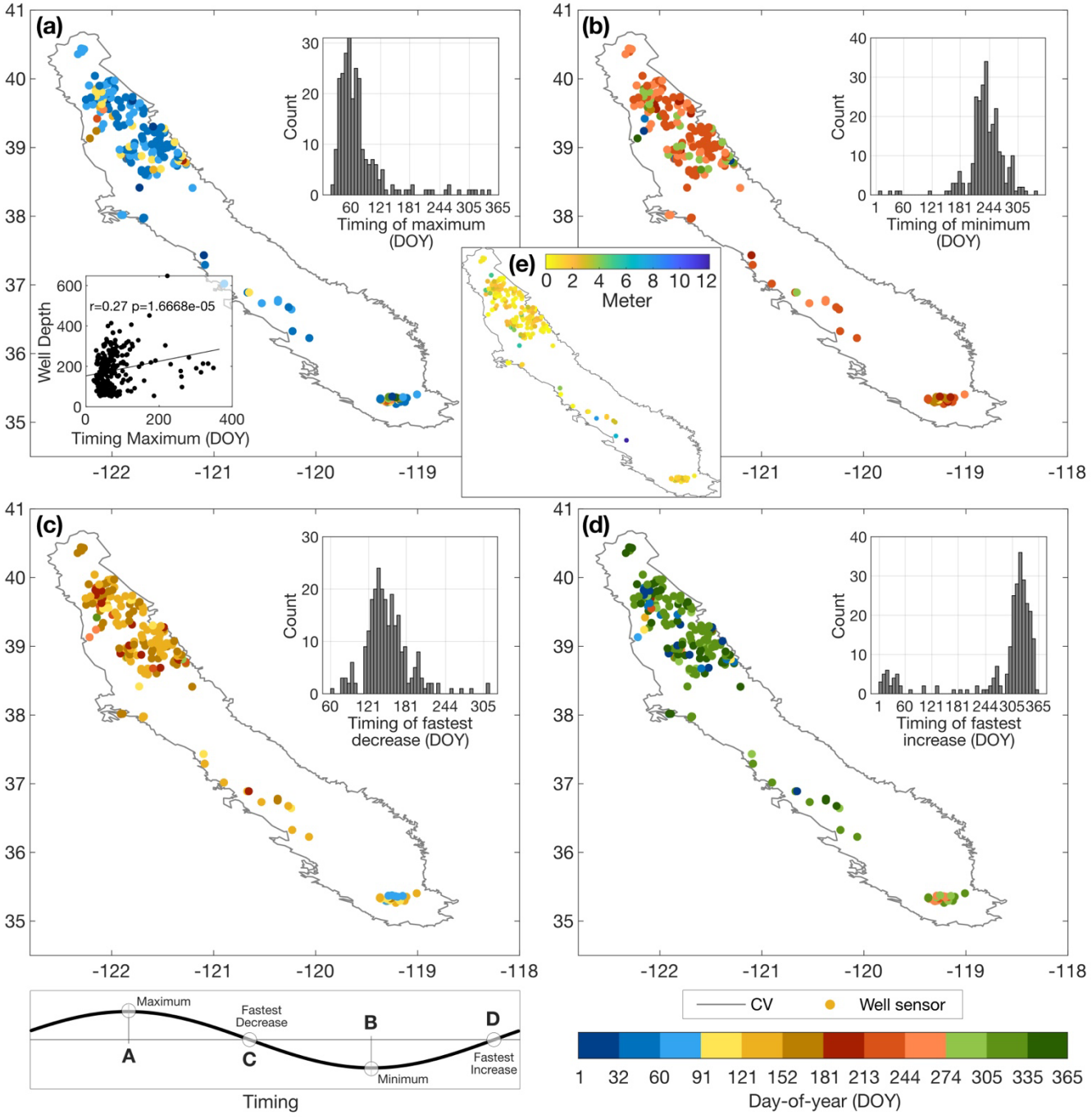

Figure S8. Annual signal parameter of groundwater levels. Timing of annual groundwater level variations (median DOY of peak time during respective observation period). Timing of extremes in annual groundwater level variations at deepest sensor with depth of below 50 m throughout the Central Valley, and corresponding histogram, for (a) maximum groundwater level occurring during winter, (b) minimum groundwater level during summer, (c) fastest groundwater level decrease during spring, and (d) fastest groundwater level increase during fall. (e) Shows the estimated seasonal amplitude at each site.

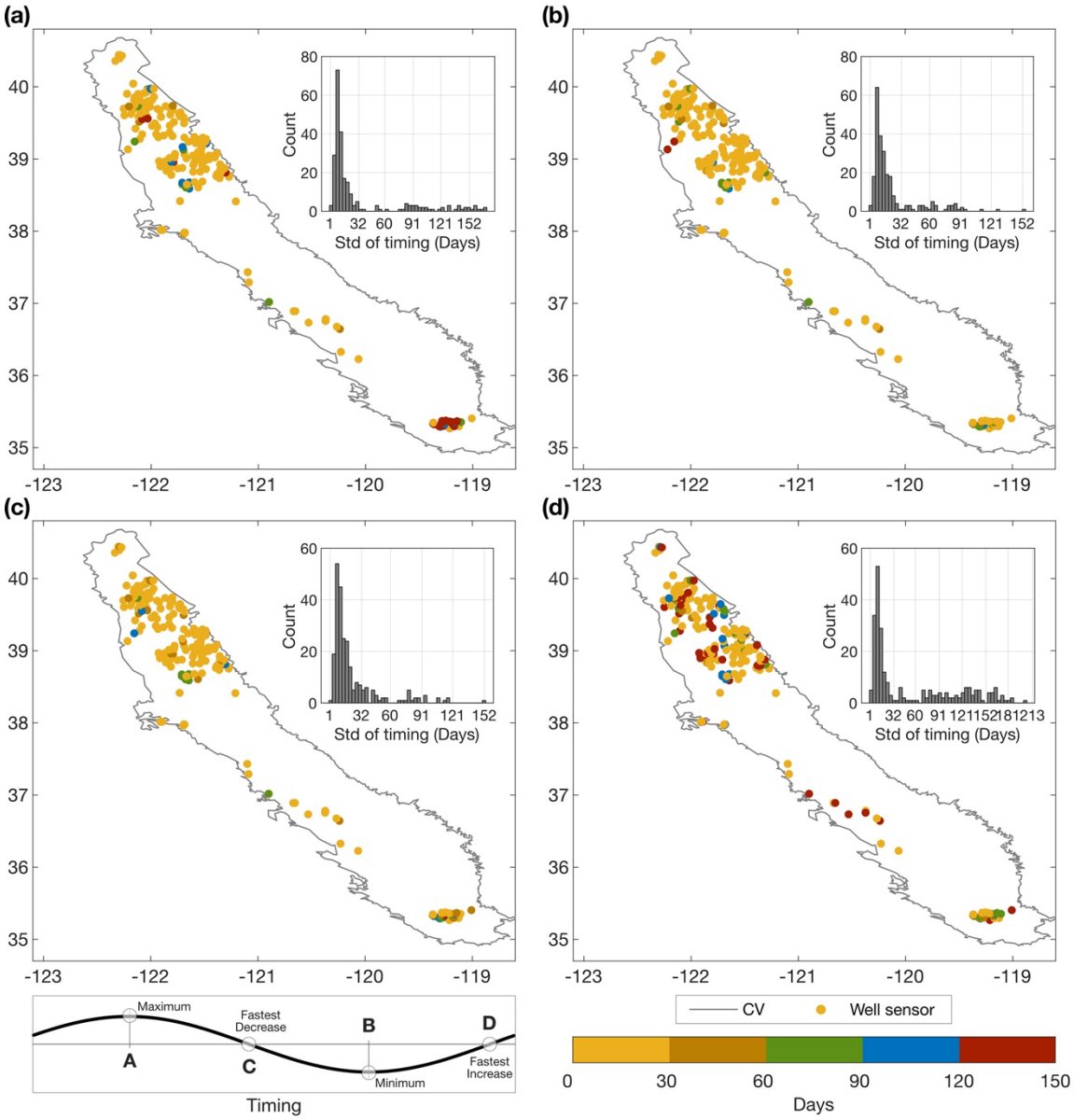

Figure S9. Standard deviation of timing of annual groundwater level variations. Standard deviation (std) of the year-to-year timing of seasonal variations in available groundwater records from observation wells shown in Fig. S8, and corresponding histogram, for (a) maximum groundwater level, (b) minimum groundwater level, (c) fastest groundwater level decrease, and (d) fastest groundwater level increase. A small standard deviation indicates very regular timing of the oscillation between maximum and minimum groundwater level each year, during the years on record.

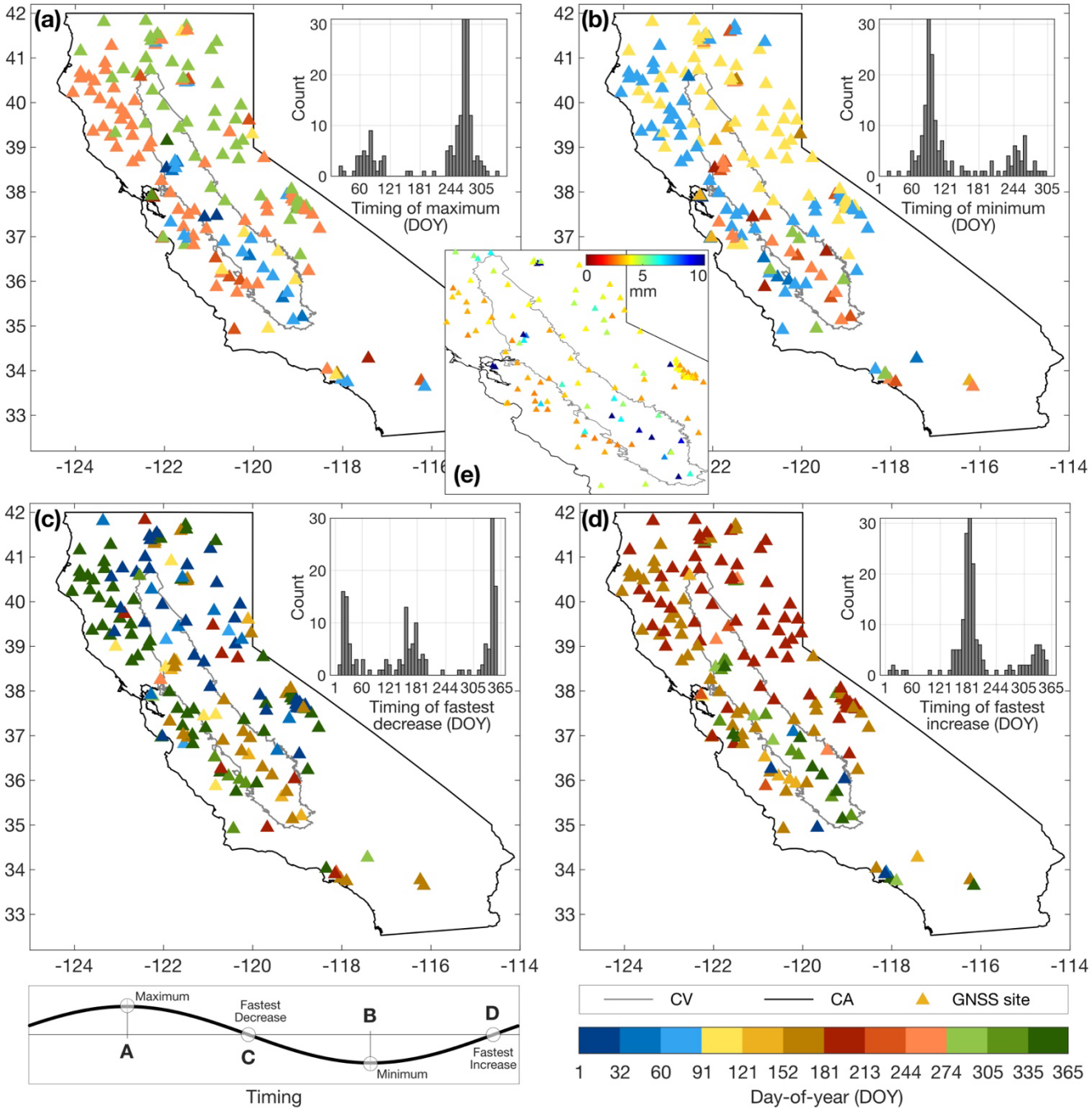

Figure 10. Annual signal parameter of GNSS deformation time series. Timing of annual vertical land motion (VLM). Timing of extremes in annual VLM at GNSS sites throughout California, and corresponding histogram, for (a) maximum VLM, (b) minimum VLM, (c) fastest decrease of VLM, and (d) fastest increase of VLM. (e) Shows the estimated seasonal amplitude at each site.

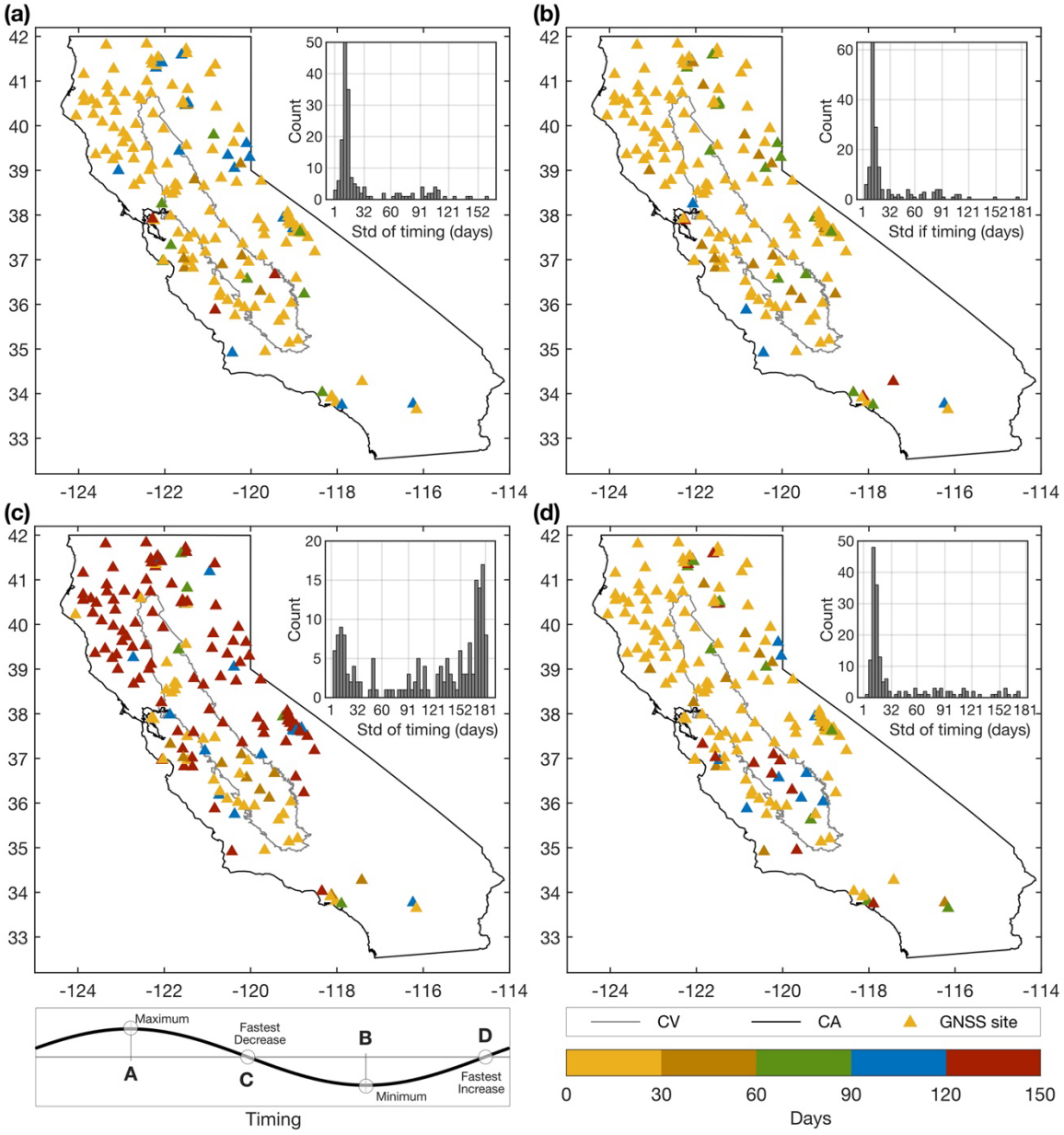

Figure S11. Standard deviation of timing of annual vertical land motion. Standard deviation (std) of the year-to-year timing of seasonal variations in vertical land motion at GNSS sites shown in Fig. S10, and corresponding histogram, for (a) maximum VLM, (b) minimum VLM, (c) fastest VLM decrease, and (d) fastest VLM increase. A small standard deviation indicates very regular annual oscillation between uplift and subsidence each year, during the years on record.

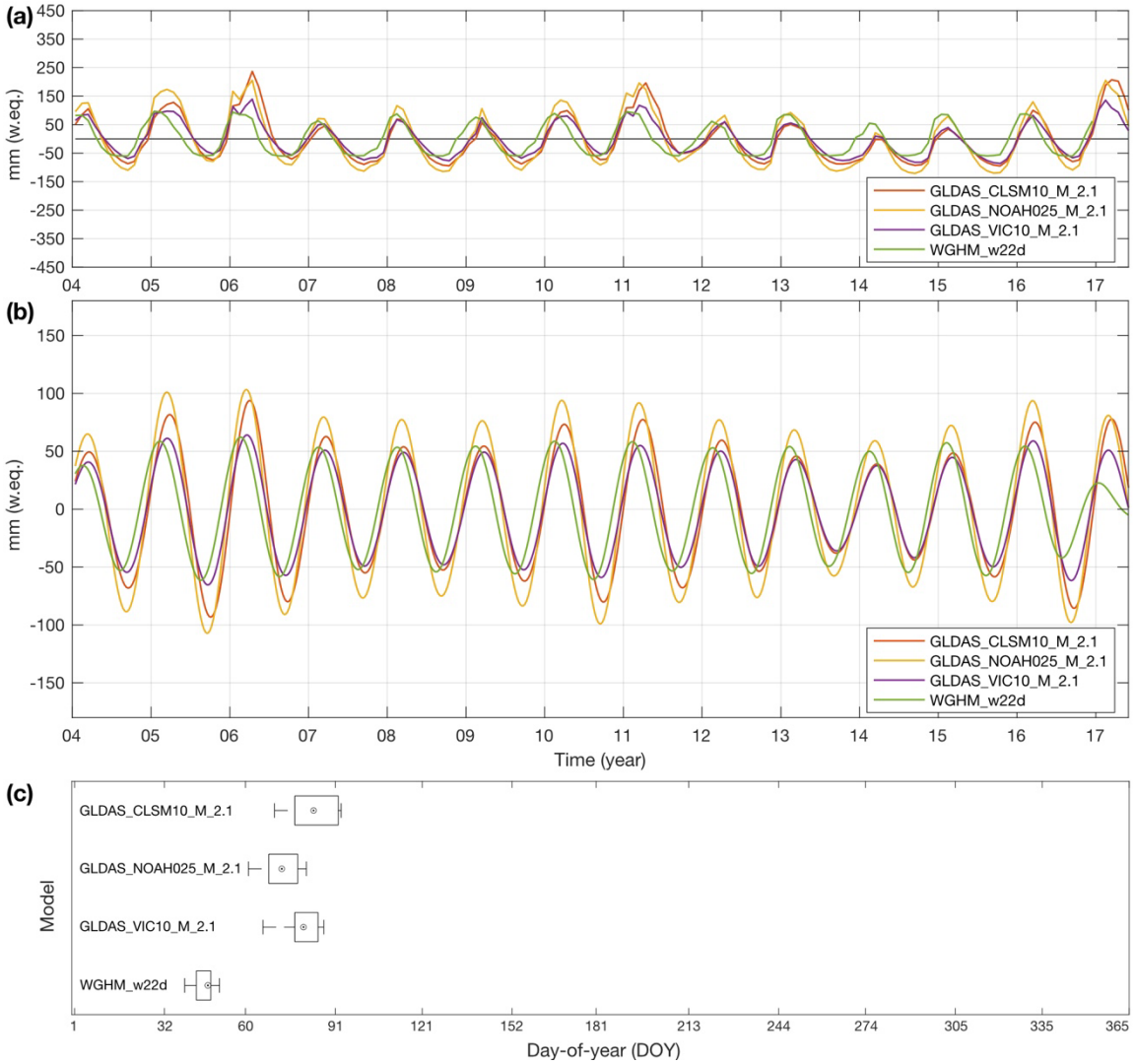

Figure S12. Soil storage variations from different hydrological models. (a) Monthly time series of soil moisture variation from four global hydrological models (GLDAS-CLSM, -NOAH, -VIC and WGHM), (b) corresponding reconstructed annual signal component after wavelet analysis at daily sampling resolution, and (c) timing of the maximum of the annual signal in day-of-year (DOY).

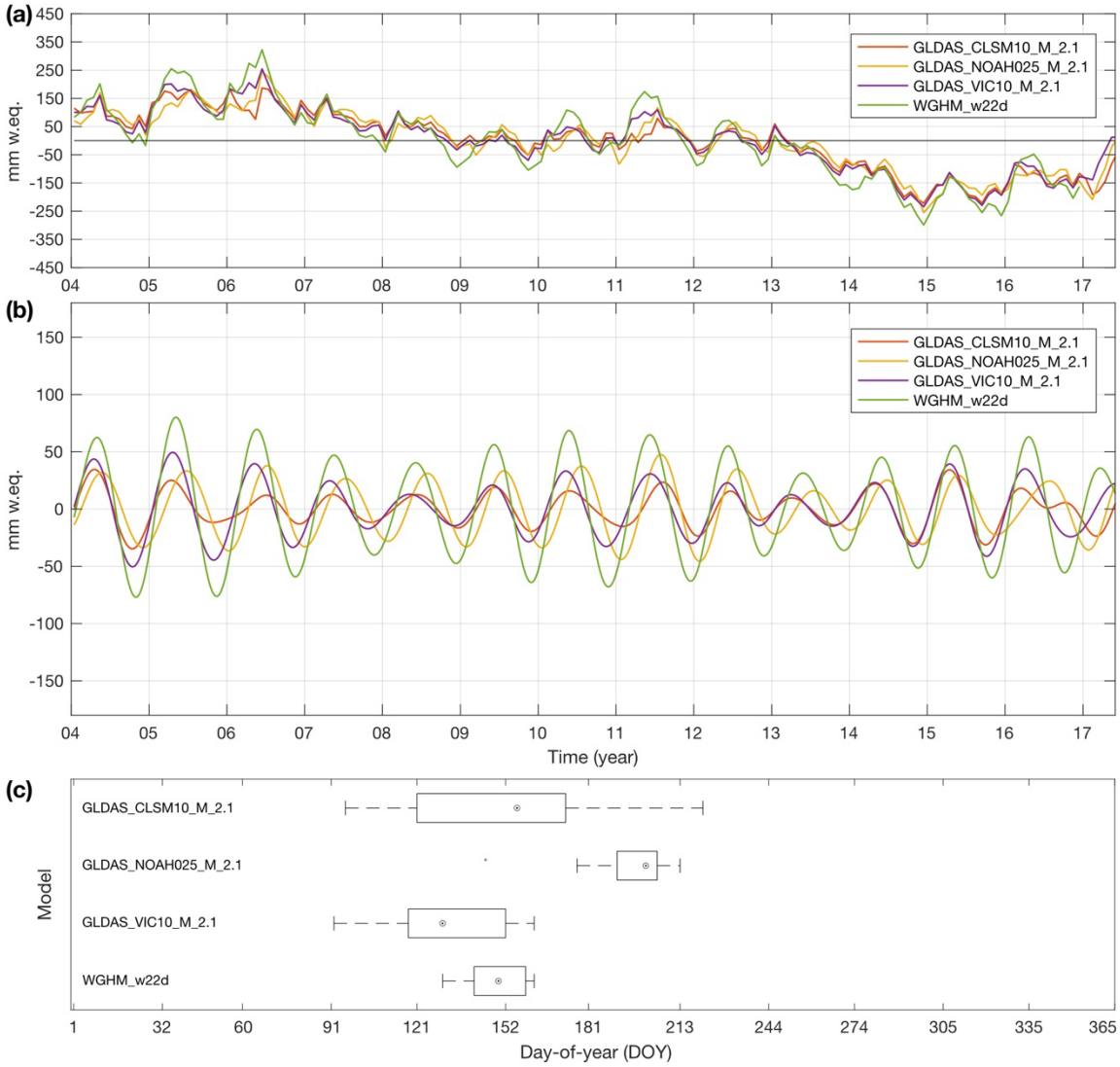

Figure S13. Groundwater storage variations from different hydrological models. (a) Monthly time series of groundwater storage variations calculated from four different global hydrological models (GLDAS-CLSM, -NOAH, -VIC and WGHM) (shown in Fig. S12) and further hydrology (variations in total, surface and snow water as shown in Fig. 1c), (b) corresponding reconstructed annual signal component after wavelet analysis at daily sampling-resolution, and (c) timing of the maximum of the annual signal in day of year.

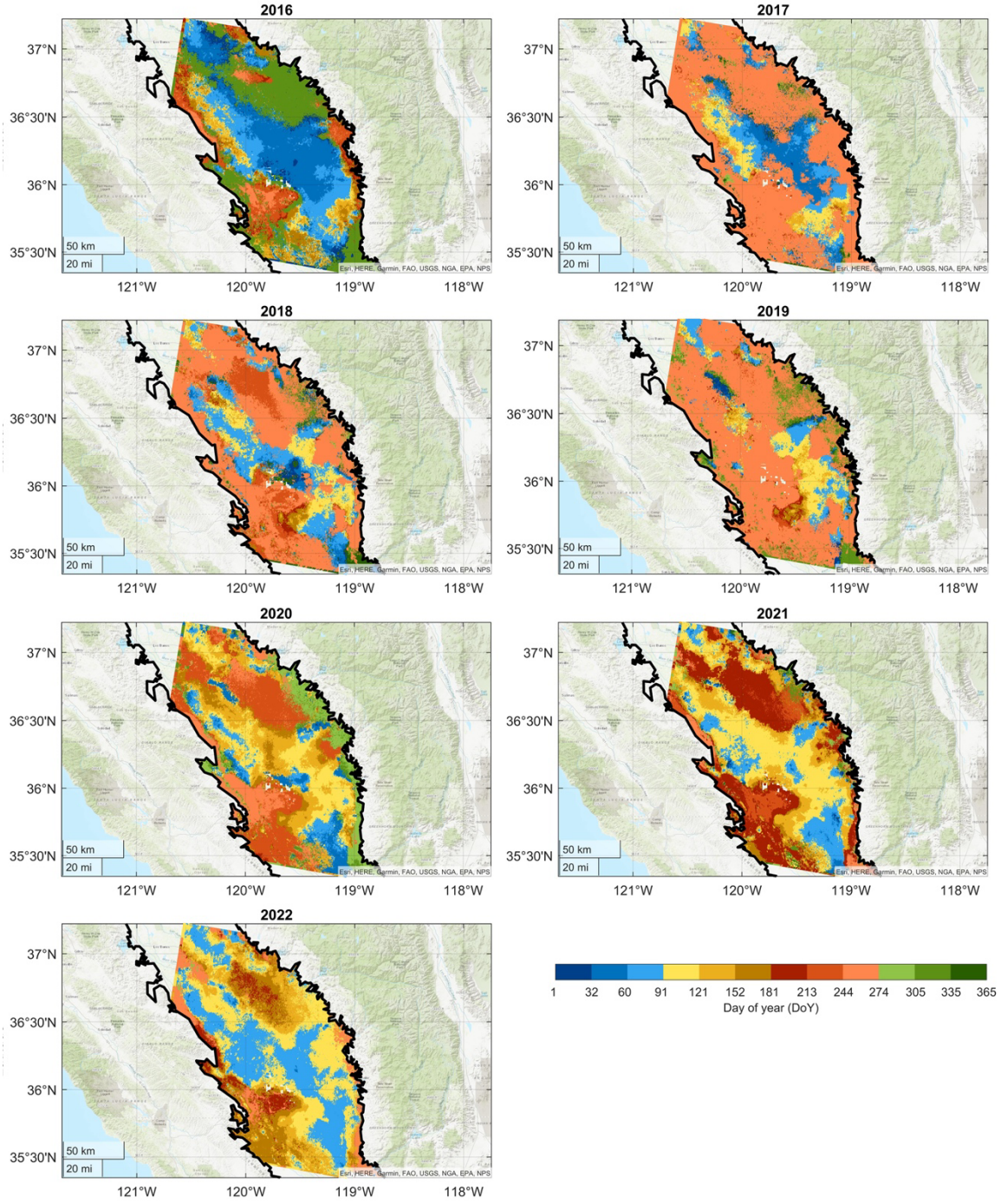

Figure S14. Yearly annual phase (median DOY of peak LOS) of InSAR deformation time series for years 2016-2022 derived from an InSAR deformation time series during the exact period of 11/27/2015 to 12/20/2022.

205

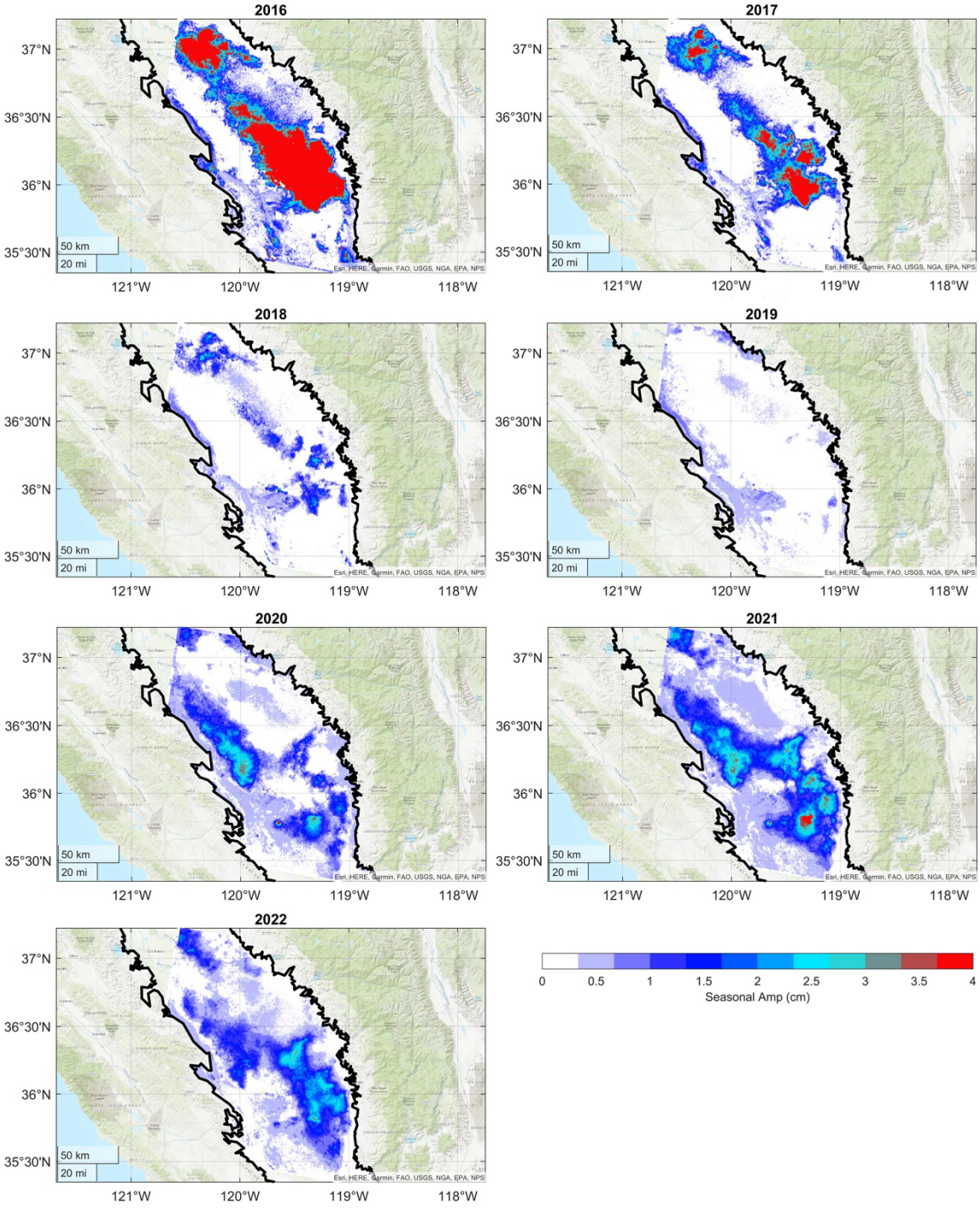

Figure S15. Yearly annual amplitude of InSAR deformation time series for years of 2016-2022 derived from an InSAR deformation time series during the exact period of 11/27/2015 to 12/20/2022..

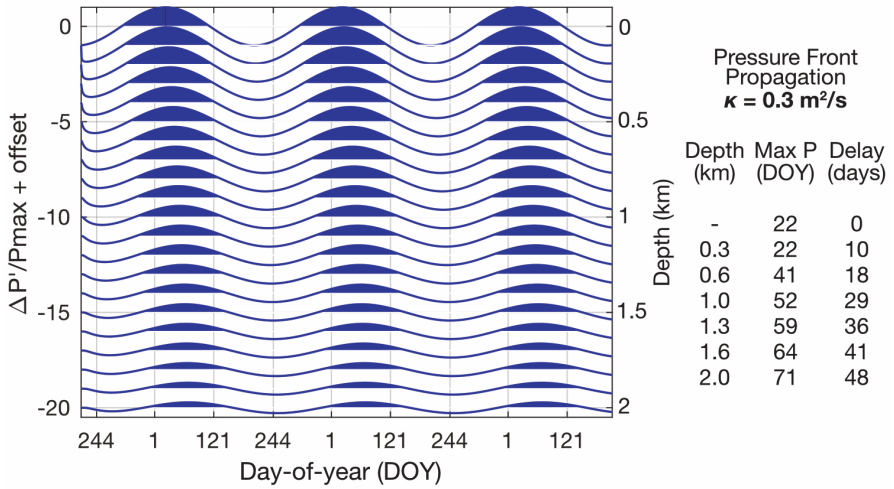

Figure S16. Vertical pressure propagation for elevation difference between the Sierra Nevada and the Central Valley aquifers. Normalized pressure change ($\Delta P'/P_{max}$) at different depths due to standard 1D calculation of pressure front propagation along mountain block recharge conduits in the fractured bedrock of the Sierra Nevada. Graphs are incrementally offset by -1 for each depth. In top groundwater layers, maximum pressure occurs on January 22nd (DOY 22), which is driven by mean annual water availability in the recharge area (Fig. 6b). The table to the right indicates DOY and time delay of the pressure propagation to a depth of 300-2000 m. Given a hydraulic diffusivity $\kappa = 0.3\ m^2/s$ (reasonable for fractured granite bedrocks), the pressure front needs ~0.6 (1.2, 1.6) months to propagate to a depth of 600 (1300, 2000) m. A smaller hydraulic diffusivity would lead to a slower propagation to depth and vice versa, examples for $\kappa = 0.5, 0.1\ m^2/s$ are shown in Figure S17.

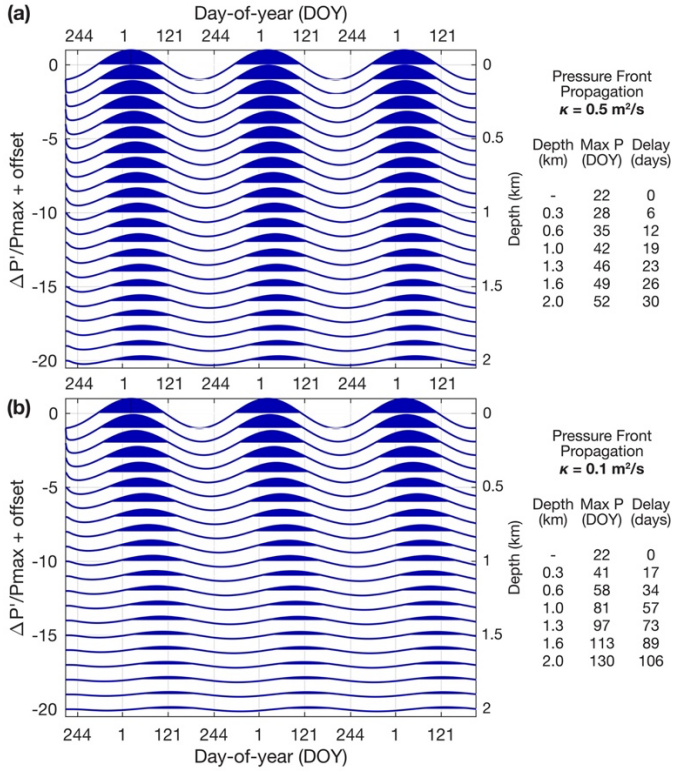

Figure S17. Same as Figure S16, but for hydraulic diffusivity (a) κ = 0.5 m2/s, (b) κ = 0.1 m2/s.

References

Bales, R. C., Hopmans, J. W., O'Geen, A. T., Meadows, M., Hartsough, P. C., Kirchner, P., Hunsaker, C. T., & Beaudette, D. (2011). Soil Moisture Response to Snowmelt and Rainfall in a Sierra Nevada Mixed-Conifer Forest. *Vadose Zone Journal*, *10*(3), 786–799. https://doi.org/10.2136/vzj2011.0001

Fetter, C. W., & Kreamer, D. (2022). *Applied Hydrogeology* (5th ed.). Waveland Press.

Gao, S. S., Silver, P. G., Linde, A. T., & Sacks, I. S. (2000). Annual modulation of triggered seismicity following the 1992 Landers earthquake in California. *Nature*, *406*(6795), 500–504. https://doi.org/10.1038/35020045

Montgomery-Brown, E. K., Shelly, D. R., & Hsieh, P. A. (2019). Snowmelt-Triggered Earthquake Swarms at the Margin of Long Valley Caldera, California. *Geophysical Research Letters*, *46*(7), 3698–3705. https://doi.org/10.1029/2019GL082254

Ojha, C., Shirzaei, M., Werth, S., Argus, D. F., & Farr, T. G. (2018). Sustained Groundwater Loss in California's Central Valley Exacerbated by Intense Drought Periods. *Water Resources Research*, *54*(7), 4449–4460. https://doi.org/10.1029/2017WR022250

Saar, M. O., & Manga, M. (2003). Seismicity induced by seasonal groundwater recharge at Mt. Hood, Oregon. *Earth and Planetary Science Letters*, *214*(3–4), 605–618. https://doi.org/10.1016/S0012-821X(03)00418-7

Talwani, P., & Acree, S. (1985). Pore pressure diffusion and the mechanism of reservoir-induced seismicity. In *Earthquake prediction* (pp. 947–965). Springer.

Urióstegui, S. H., Bibby, R. K., Esser, B. K., & Clark, J. F. (2017). Quantifying annual groundwater recharge and storage in the central Sierra Nevada using naturally occurring 35S. *Hydrological Processes*, *31*(6), 1382–1397. https://doi.org/10.1002/hyp.11112

Viswanathan, H. S., Ajo-Franklin, J., Birkholzer, J. T., Carey, J. W., Guglielmi, Y., Hyman, J. D., Karra, S., Pyrak-Nolte, L. J., Rajaram, H., Srinivasan, G., & Tartakovsky, D. M. (2022). From Fluid Flow to Coupled Processes in Fractured Rock: Recent Advances and New Frontiers. In *Reviews of Geophysics* (Vol. 60, Number 1). John Wiley and Sons Inc. https://doi.org/10.1029/2021RG000744

Wang, H. F. (2000). *Theory of Linear Poroelasticity with Applications to Geomechanics and Hydrogeology*. Princeton Univ. Press.